Title

Polarized endosome dynamics engage cytoplasmic Par-3 that recruits dynein during asymmetric cell division

Journal

Science Advances, 7(24)

ISSN

2375-2548

Authors

Zhao, Xiang
Garcia, Jason Q
Tong, Kai
et al.

Publication Date

2021-06-11

DOI

10.1126/sciadv.abg1244

Peer reviewed

DEVELOPMENTAL NEUROSCIENCE

Polarized endosome dynamics engage cytoplasmic Par-3 that recruits dynein during asymmetric cell division

Xiang Zhao[1], Jason Q. Garcia[1,2], Kai Tong[1,3†], Xingye Chen[4], Bin Yang[4,5], Qi Li[4,6], Zhipeng Dai[1], Xiaoyu Shi[4‡], Ian B. Seiple[4,6], Bo Huang[4,5], Su Guo[1,2,7*]

In the developing embryos, the cortical polarity regulator Par-3 is critical for establishing Notch signaling asymmetry between daughter cells during asymmetric cell division (ACD). How cortically localized Par-3 establishes asymmetric Notch activity in the nucleus is not understood. Here, using in vivo time-lapse imaging of mitotic radial glia progenitors in the developing zebrafish forebrain, we uncover that during horizontal ACD along the anteroposterior embryonic axis, endosomes containing the Notch ligand DeltaD (Dld) move toward the cleavage plane and preferentially segregate into the posterior (subsequently basal) Notch^{hi} daughter. This asymmetric segregation requires the activity of Par-3 and dynein motor complex. Using label retention expansion microscopy, we further detect Par-3 in the cytosol colocalizing the dynein light intermediate chain 1 (Dlic1) onto Dld endosomes. Par-3, Dlic1, and Dld are associated in protein complexes in vivo. Our data reveal an unanticipated mechanism by which cytoplasmic Par-3 directly polarizes Notch signaling components during ACD.

INTRODUCTION

Progenitor cells need to properly balance self-renewal and differentiation. Asymmetric cell division (ACD) is an important means to impart these distinct potentials to different daughter cells. Defects in ACD are associated with diseases such as cancer and developmental disorders (*1*–*4*). Therefore, elucidating the mechanisms that regulate ACD is not only fundamental for understanding basic biology but also critical for elucidating disease etiology and devising therapeutic strategies.

In metazoans, partitioning-defective (Par) protein complexes, originally found in *Caenorhabditis elegans* (*5*–*7*), are evolutionarily conserved regulators of cell polarity and ACD (*8*–*12*). Among them, Par-3 (also called PARD3, Bazooka) has been studied in the context of neural progenitor self-renewal and differentiation from *Drosophila* to mammals (*13*–*22*). During ACD in both invertebrate and vertebrate neural progenitors, Par-3 displays asymmetric cortical localization and is required to establish, between daughter cells, the asymmetric activity of Notch signaling (Notch^{hi} versus Notch^{lo}) (*20*, *23*–*28*), a key regulator of cell fate decisions (*29*, *30*). Despite these advances, it is not known how Par-3, thought to regulate polarity exclusively through its oligomeric scaffolding properties at the cortex (*31*), leads to differential Notch activity in the nuclei of daughter cells.

Here, we addressed this question in the context of radial glia progenitors (RGPs) of the developing zebrafish forebrain. RGPs are the principal vertebrate neural stem cells (*32*, *33*). During active neurogenesis in the developing zebrafish forebrain, most of the RGPs undergo ACD (*20*). Using an antibody uptake assay (*34*) coupled with in vivo time-lapse imaging, we visualized the dynamics of internalized Notch ligand DeltaD (Dld) during RGP ACD. Internalized Dld was not observed in the *mind bomb* (*mib*) mutant that disrupts an evolutionarily conserved E3 ubiquitin ligase essential for Notch ligand endocytosis (*35*), suggesting that internalized Dld represents Dld endosomes. Despite the heterogeneity of RGP division modes, we observed a consistent convergent movement of Dld endosomes toward the emerging cleavage plane followed by preferential segregation into the posterior (subsequently basal) Notch^{hi} daughter. Such polarized endosome segregation was critically dependent on the activity of *par-3* and dynein motor complex. Furthermore, using label retention expansion microscopy (LR-ExM), a newly developed methodology that overcomes the limitation of signal loss associated with traditional ExM (*36*), we unexpectedly detected cytoplasmic Par-3 that colocalized and was required to mediate the association of dynein light intermediate chain 1 (Dlic1) with Dld endosomes. In vivo coimmunoprecipitation showed that Par-3, Dld, and Dlic1 formed protein complexes. Together, our findings have uncovered cytoplasmic Par-3 and a direct role it has in localizing intracellular determinants.

RESULTS

In vivo time-lapse imaging reveals polarized dynamics of Notch ligand–containing endosomes in horizontally dividing RGPs

As shown previously, in the developing zebrafish forebrain, most of the RGPs undergo ACD to generate an apical differentiating daughter with low Notch activity and a basal self-renewing daughter with high Notch activity (*20*). To understand how such Notch signaling asymmetry arises, we visualized internalized Notch ligand Dld using an antibody uptake assay (*34*) and in vivo time-lapse imaging. Intriguingly, only punctate cytoplasmic labeling was observed (Fig. 1A); no Dld was accumulated on the plasma membrane of mitotic RGPs. In the *mib* mutant, which disrupts a conserved ubiquitin E3 ligase

[1]Department of Bioengineering and Therapeutic Sciences, University of California, San Francisco, San Francisco, CA 94143, USA. [2]Tetrad Graduate Program, University of California, San Francisco, San Francisco, CA 94143, USA. [3]State Key Laboratory of Genetic Engineering, Department of Genetics, School of Life Sciences, Fudan University, Shanghai, China. [4]Department of Pharmaceutical Chemistry, University of California, San Francisco, San Francisco, CA 94143, USA. [5]Chan Zuckerberg Biohub, San Francisco, CA 94143, USA. [6]Cardiovascular Research Institute, University of California, San Francisco, San Francisco, CA 94143, USA. [7]Programs in Human Genetics and Biological Sciences, University of California, San Francisco, San Francisco, CA 94143, USA.
*Corresponding author. Email: su.guo@ucsf.edu
†Present address: School of Biological Sciences, Georgia Institute of Technology, Atlanta, GA 30332, USA.
‡Present address: Department of Developmental and Cell Biology, University of California, Irvine, Irvine, CA 92697, USA.

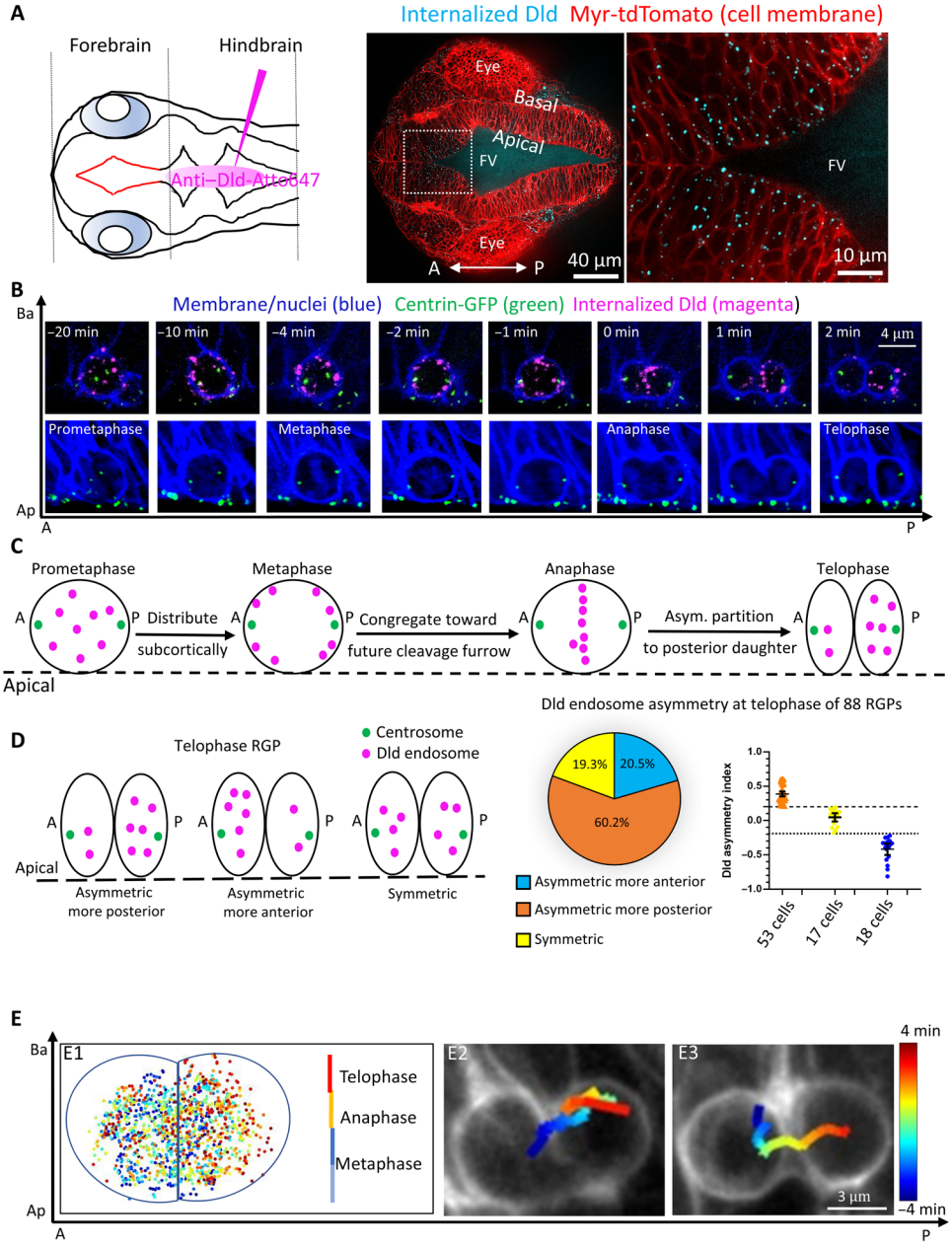

Fig. 1. Polarized dynamics of Notch ligand–containing endosomes during RGP division. (**A**) Schematic diagram of a 28-hpf embryo (dorsal view) indicating the site of anti-Delta D-Atto647N (Dld) antibody injection (left). Right: Internalized Dld (blue) imaged 2 hours after antibody injection shows punctate appearance in RGPs (membrane labeled red). FV, forebrain ventricle. (**B**) Time-lapse imaging of mitotic RGP showing the dynamics of labeled Dld endosomes. Membrane, nucleus, and centrosomes [green fluorescent protein (GFP)–centrin] are marked as shown. (**C**) Schematic diagram showing typical phases of internalized Dld dynamic patterns in (B). (**D**) Schematic diagrams and statistics of distribution patterns of Dld endosomes in telophase RGPs (see Materials and Methods for the quantification of asymmetry index). Dotted lines in the scatter plot denote the asymmetric threshold of |0.2|. $n = 88$ RGPs, from 20 embryos of six experiments. (**E**) Automated tracking of Dld endosomes. (E1) Plot of time-lapse data from a composite of 19 RGPs. Each dot represents a tracked endosome at a given time. Color codes for cell cycle stages. The blue vertical line denoting the midpoint between two centrosomes is used for image registration. (E2 and E3) The plot trajectory of a singly labeled Dld endosome in two RGPs. Time is registered and color-coded (anaphase, $T = 0$). A-P, anteroposterior; Ap-Ba, apicobasal. In all images/plots, maximum intensity projection (MIP) of 5-μm z-stacks (1-μm z-step) is shown. The time interval between each z-stack is 12 s.

essential for Notch ligand endocytosis (*35*), the punctate cytoplasmic labeling of Dld was, however, lost; fluorescence was instead largely concentrated on the plasma membrane (fig. S1A). These data indicate that the punctately labeled structures are internalized Dld in endosomes (in short, Dld endosomes). They also suggest that, in mitotic RGPs, Dld undergoes active endocytosis to be predominantly distributed in endocytic vesicles. We also evaluated whether this labeling method affected embryonic development or RGP cell division modes. The developing forebrain RGPs at this developmental stage predominantly undergo horizontal division

(with the division axis parallel to the ventricular surface). No substantial differences in embryonic morphology and RGP division modes were observed between control and Dld antibody-injected embryos (fig. S1, B to D).

To observe in vivo Dld endosome dynamics during RGP divisions, we performed time-lapse imaging using 24– to 30–hours postfertilization (hpf) *Tg[ef1a-MyrTdTomato]* embryos (marking cell membranes): The centrosomes were labeled by microinjection of *GFP-centrin* mRNA at one- to four-cell stages, followed by Dld antibody injection into the forebrain ventricle at 22 hpf. The cell cycle stage of dividing RGPs was determined using *Tg[ef1a-MyrTdTomato; ef1a-H2BmRFP]* embryos, which marked both the cell membrane and nucleus, enabling a correlation between cell shape and DNA patterns (Fig. 1B; time 0 represents anaphase when incoming cleavage furrows become first visible). During imaging, both the apicobasal (Ap-Ba) and the anteroposterior (A-P) axes of RGPs were tracked. As shown in fig. S1 (C and D), most of the RGPs divided horizontally along the anteroposterior (A-P) embryonic axis. These horizontally dividing RGPs were therefore the focus of this study (theretofore referred to as RGPs unless otherwise specified). By analyzing these dynamic videos (see movie S1), we made several intriguing observations (Fig. 1, B and C, and fig. S2). Dld endosomes were distributed throughout the cytosol during prophase to prometaphase. During metaphase, most Dld endosomes appeared to be subcortical. By anaphase, however, most Dld endosomes congregated toward the future cleavage plane and subsequently were unequally partitioned into the posterior daughter after division. Using asymmetry indices with a threshold of |0.2| as previously described (*25*, *27*), we quantitatively analyzed the distribution of internalized Dld in 88 RGPs at the telophase stage when two daughter cells were clearly discernible. The results showed that most (60.2%) of the RGPs asymmetrically partitioned Dld endosomes into the posterior daughter. Some RGPs with symmetric or anteriorly enriched Dld endosomes were also observed (Fig. 1D; see Materials and Methods for the quantification of asymmetry index), likely reflecting the heterogeneity of in vivo RGP behavior or alternatively representing, in part, the noise in the system due to mosaic Dld labeling. These observed RGPs, whether symmetrically or asymmetrically partitioned Dld endosomes, were distributed around the forebrain ventricle in an intermingled manner (fig. S3).

We next performed automated tracking analysis of 19 RGPs, which were captured throughout their entire mitotic cell cycle (from prophase to telophase) and, moreover, with consistent tracking of Dld endosomes in all frames. Tracking of more than 300 Dld endosomes from all 19 cells throughout the RGP mitotic cycle (45 time points) allowed us to visualize the progressive enrichment of endosomes toward the posterior daughter [Fig. 1E (E1) and movie S2]. Such enrichment could be due to directional endosome movement toward the posterior, their selective degradation at the anterior, or both. The presence of supernumerary-labeled Dld endosomes made it challenging to unambiguously discern individual endosome's trajectories. Intriguingly, because of the mosaic nature of our Dld-labeling method, some RGPs contained only a single labeled Dld endosome. This enabled us to clearly track the movement of individual endosomes. We observed that the Dld endosome first moved toward the cleavage plane, followed by a directed maneuver toward the posterior side [Fig. 1E (E2 and E3) and movies S3 to S6]. Together, these data uncover polarized dynamics of Dld endosomes during horizontal RGP division and show that Dld endosomes are asymmetrically segregated into the posterior daughter in most of the RGP divisions.

Notch ligand–containing endosomes preferentially segregate to the posterior (subsequently basal) Notch^{hi} daughter

We next asked what the possible outcome of the daughter that received a higher amount of Dld endosomes is: Will it be Notch^{hi} or Notch^{lo}? Previous studies have shown that Notch^{hi} versus Notch^{lo} is an outcome of ACD and can be used as a proxy for self-renewing versus differentiating potential in daughter cells of embryonic RGP ACD (*20*, *26*, *27*). On the basis of a previous study using the *Drosophila* sensory organ precursor (SOP) system, which has uncovered the copresence of Delta and Notch in the same endosomes (*23*), we wondered whether the daughter with higher amount of Dld would also have higher amount of Notch activity (i.e., Notch^{hi}) (Fig. 2A).

Because of the lack of an anti-Notch antibody that works in zebrafish, we took three different approaches to address this question. First, most RGPs that we imaged in the developing zebrafish neurogenic forebrain undergo horizontal divisions along the A-P axis (fig. S1, C and D). Shortly after division, daughter cells begin interkinetic nuclear migration and adopt differential position along the apicobasal (Ap-Ba) axis. The basal daughter is previously shown to be Notch^{hi} (Fig. 2B, left) (*20*). We therefore determined the relationship between the A-P daughter position immediately following RGP mitosis and the Ap-Ba daughter position shortly thereafter. Among 42 pairs of daughter cells with observable differences in their position along the Ap-Ba axis, most (67%) had more Dld in the posterior daughter that initiated an earlier basal migration (Fig. 2B, right). These results suggest that Dld endosomes are preferentially segregated to the posterior daughter, which later becomes the basal Notch^{hi} daughter.

The second approach to discern the relationship between Dld endosome segregation and Notch activity involved analysis of the E3 ubiquitin ligase Mib, which is asymmetrically segregated to the apical-differentiating daughter following RGP ACD in zebrafish (*20*). Similar observations are also reported in the chick neural progenitors (*37*). By simultaneously tracking Dld endosomes and Mib distribution in 25 RGPs, we found that they were largely segregated into different daughter cells (Fig. 2C, fig. S4, and movie S7): 64% RGPs had anteriorly enriched Mib while posteriorly enriched Dld (Fig. 2D). Note that Mib–green fluorescent protein (GFP) showed anterior enrichment early on during the cell cycle, when Dld distribution appeared random. While this observation implied a potential asymmetric endocytosis, it does not appear to contribute to Dld asymmetry as internalized Dld appeared randomly distributed in RGPs during prometaphase. Together, this observation supports the notion that Dld endosomes preferentially segregate to the posterior-then-basal Notch^{hi} daughter and away from the Mib-high apical daughter.

Last, we performed in vivo clonal time-lapse imaging of internalized Dld in *Tg[her4.1-dRFP]* embryos, which express the Notch activity reporter (*her4.1-dRFP*) in RGPs. Because this reporter line does not label forebrain RGPs well (*38*), we performed the analysis in the developing anterior hindbrain as we have done previously (*20*). For clonal labeling of RGPs, GFP-containing DNA constructs were delivered via brain ventricle–targeted electroporation (*39*). Dld antibody was then microinjected into the brain ventricle to

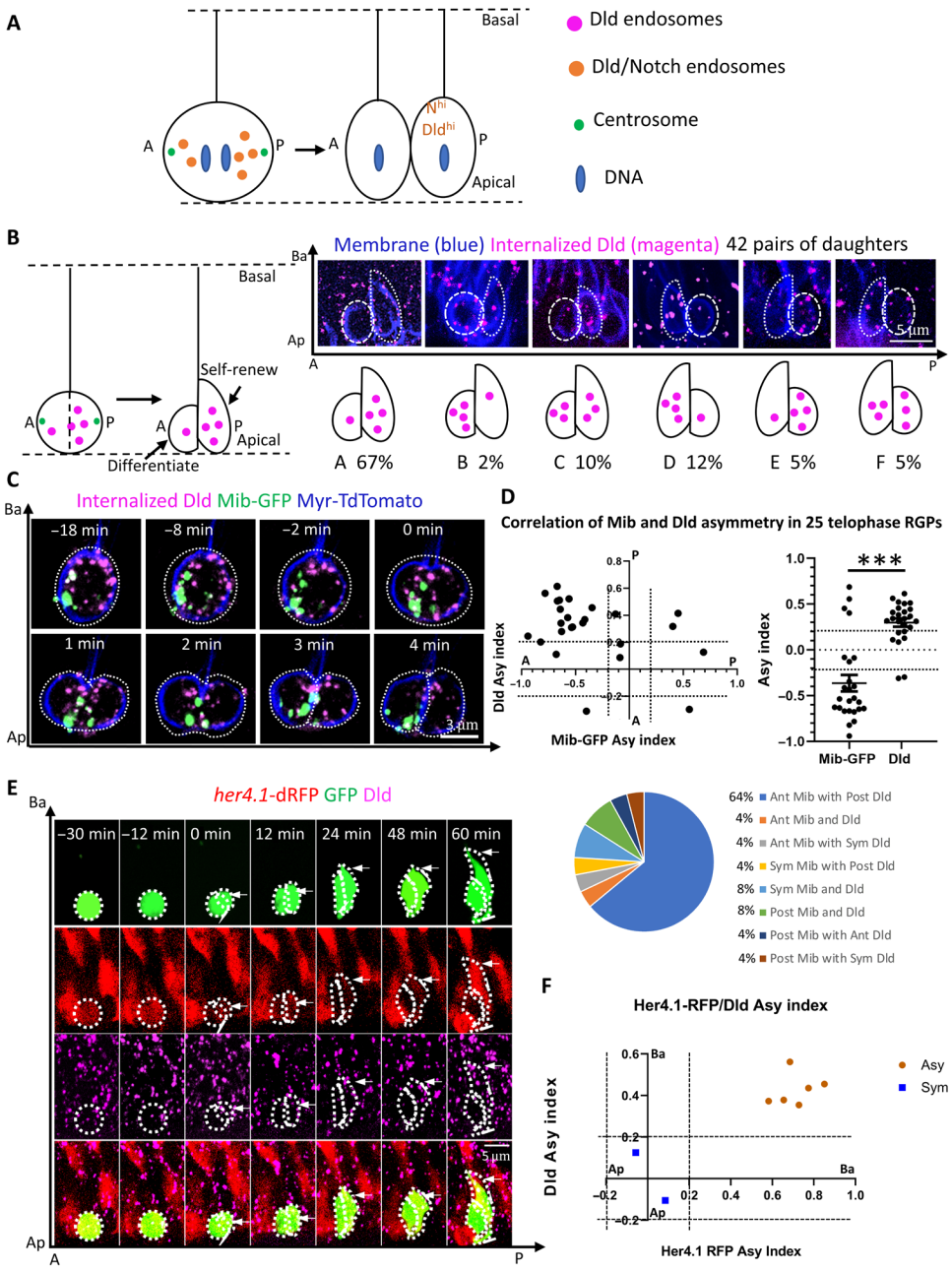

Fig. 2. Dld endosomes are preferentially segregated into the Notch^{hi} daughter following RGP division. (**A**) Schematic depicting the asymmetry of Dld endosomes (Dld^{hi}) and Notch activity (N^{hi}) in daughter cells. (**B**) Topology and statistics of relative daughter cell position along A-P (anteroposterior) and Ap-Ba (apicobasal) axes after horizontal division. MIP of 5-μm z-stacks (1-μm z-step) is shown. (**C**) Time-lapse images showing that Dld endosomes and Mib are segregated into different daughter cells following RGP division (n = 25). MIP of 5-μm z-stacks (1-μm z-step) is shown. The time interval between z-stacks is 20 s, and the total acquisition time is 30 min. (**D**) The top left graph plots individual RGP's asymmetry indices for Mib-GFP (x axis) and internalized Dld (y axis). The top right graph shows the distribution of asymmetry indices for Mib-GFP and Dld endosomes; the dotted lines indicate the threshold of |0.2| for calling asymmetry. ***P < 0.0001, t = 6.549, df = 48, n = 25; unpaired two tailed t test. Mean with SEM is shown. The bottom pie chart shows the percentage of RGPs with indicated distribution patterns. n = 25 RGPs, from eight embryos of five repeat experiments. (**E**) Time-lapse images of a clonally labeled RGP (green) showing preferential segregation of internalized Dld to *her4.1-dRFP*^{hi} daughter. MIP of 8-μm z-stacks (1-μm z-step) is shown. The time interval between z-stacks is 6 min, and the total acquisition time is ~10 hours. (**F**) Plot for quantifying *her4.1*-dRFP and internalized Dld in daughter RGPs 1 hour after anaphase. n = 8 RGPs, from eight embryos of six repeat experiments.

label internalized Dld. Three-color time-lapse imaging was subsequently carried out to simultaneously visualize RGP lineage (via sparse GFP labeling), internalized Dld (Atto647), and Notch activity (*her4.1-dRFP*). Eight RGPs were analyzed: In six of eight RGPs, *her4.1-dRFP* asymmetry was evident in daughter cells around 1 hour after anaphase. In these RGPs, Dld endosomes were found to be enriched in the daughter cell that had more *her4.1-dRFP* signal. By tracing the distribution of Dld endosomes throughout the cell

cycle, one could see that Dld endosomes became progressively enriched toward the posterior followed by segregation into the posterior daughter, which later assumed a more basal position and with higher *dRFP* fluorescence (i.e., higher Notch activity) (Fig. 2, E and F, and movie S8). In two of eight RGP lineages, *her4.1-dRFP* appeared symmetric in daughter cells, which also bore no asymmetry of Dld endosomes (Fig. 2F and fig. S5). Together, our findings suggest that the daughter cell receiving more Dld endosomes are Notch^{hi}, thereby supporting the notion that Dld endosomes might contain both the ligand and receptor and hence can be considered as Notch signaling endosomes.

Par-3 and dynein are essential for polarized dynamics of Dld endosomes

Par-3, an evolutionarily conserved cell polarity regulator that is asymmetrically distributed on the cell cortex (*40*), plays a critical role in establishing Notch signaling asymmetry in daughter cells of RGP ACD (*20*), but the underlying mechanisms are unclear. To determine whether Par-3 is involved in polarizing the dynamics of Notch signaling endosomes, we disrupted the activity of the zebrafish orthologous gene *pard3ab* (theretofore referred to as *par-3*) via microinjection of a well-established antisense morpholino oligonucleotide (MO) (*19*, *20*, *41*). Despite the fact that a maternal zygotic germline *pard3ab* knockout has been previously generated, it has grossly normal brain morphology and survives largely to adulthood (*42*). This phenotype is distinct from defective brain morphology and abnormal proliferation/differentiation states observed in the morphants, suggesting that genetic compensation (*43*) is at play. Therefore, this knockout line is deemed unsuitable for our study.

Imaging of internalized Dld in *par-3* morphants uncovered that, while Dld endosomes underwent largely normal subcortical association and congregation toward the future cleavage plane, their final asymmetric segregation into the posterior daughter was significantly disrupted (Fig. 3, B and E to G, and movie S9). This defect was rescuable by Par-3-GFP mRNA injection (fig. S6). These data, together with the observed knockdown of Par-3 protein in RGPs (fig. S8), validate the MO specificity and efficacy in our system and suggest that Par-3 is essential for polarized segregation of Notch signaling endosomes during RGP ACD.

Previous studies in *Drosophila* SOPs have uncovered a critical role of plus-end kinesin motors in the initial targeting of Notch signaling endosomes toward the cleavage plane (*24*). However, motor involvement in the later asymmetric segregation step is not known. In dividing zebrafish RGPs, we observed directed movements of Dld endosomes toward the posterior, which implies that the final polarization process might also be motor dependent. We therefore examined whether minus-end dynein motors might play a role. The pharmacological dynein inhibitor ciliobrevin D (CBD) was applied to zebrafish embryos at a concentration that still enabled RGP cell division. In CBD-treated RGPs, we observed that the Notch signaling endosomes were much larger in appearance as if they "collided" into one another. These "enlarged" endosomes remained at the cleavage furrow throughout the division (Fig. 3, C and E to G, and movie S10).

We next sought to genetically test the involvement of dynein in the polarized dynamics of Notch signaling endosomes by investigating the role of *dync1li* (*dynein cytoplasmic 1 light intermediate chain*, also referred to as *dlic*) genes. This experiment was motivated by a previous study reporting an interaction between DLIC2 and Par-3 in cultured NIH 3T3 cells (*44*). While invertebrates have a single *dlic* gene (*45*, *46*), vertebrates have evolved to express two *dlic* genes (*dlic1* and *dlic2*), which are thought to define tissue- or cell type–specific dynein complexes (*47*). Among all the cytoplasmic dynein subunits, Dlic is the least well understood. It contains a RAS-like domain that interacts with the dynein heavy-chain and a C-terminal domain contacting activating adaptors and, in some cases, the cargo (*48*). We therefore sought to perturb *dlic1 and dlic2* activity and ask whether it would disrupt the polarized dynamics of Dld endosomes in zebrafish RGPs.

MO-mediated knockdown has certain advantages over germline knockouts. First, it circumvents the troubling genetic compensation effect (e.g., as in the case for *pard3ab*). Second, the concentration of MOs delivered to each embryo can be titrated to obtain partial knockdown, which provides an opportunity to bypass early embryonic arrests (e.g., as in the case for dynein subunit–encoding genes, which are essential for cell division). Last, MOs can be conveniently delivered into transgenic lines harboring multiple transgenes for live-imaging purposes. Getting multiple transgenes together with one or multiple homozygous germline knockout alleles in a single embryo is challenging and time-consuming. Together, MOs are effective tools for performing gene knockdowns, if proper controls for validating efficacy and specificity are included. We used established MOs that target *dlic1* and *dlic2* in zebrafish in our study (*49*). Although both MOs disrupted embryonic development (e.g., as shown by the enlarged yolk indicative of reduced growth rate; fig. S7A), only *dlic1* MO affected Dld asymmetry in mitotic RGPs (Fig. 3, D to G, and fig. S6, C to E).

To evaluate MO efficacy in the context of our system, we used an anti–Dlic-Cter antibody against the *Drosophila* isoform (*50*) because of the lack of antibodies against zebrafish Dlic1 and Dlic2. Western blotting on 24-hpf embryos detected a major band of ~54 kDa (the expected size for zDlic1 and zDlic2 proteins). This band was significantly reduced in the *dlic1* morphants but was increased in the *dlic2* morphants (fig. S7B). Furthermore, immunoreactivity was detected in mitotic RGPs, which was significantly reduced again in the *dlic1* (but not the *dlic2*) morphants (fig. S7C). This observation is consistent with the notion that the *Drosophila* anti–Dlic-Cter antibody specifically recognizes zDlic1 but not ZDlic2. These results further suggest that *dlic1* is expressed in mitotic RGPs and can be effectively knocked down by the *dlic1* MO, resulting in disrupted Dld asymmetry. However, no conclusion can be drawn from our data regarding the role of *zdlic2*, as we are unable to verify the efficacy of *dlic2* MO because of the lack of a zDlic2-specific antibody.

To further evaluate the specificity of *dlic1* MO, we microinjected MO-insensitive *dlic1* mRNA. The loss of polarized Dld endosome dynamics in *dlic1* MOs was rescued by such mRNA injection (fig. S6, B, D, and E). Together, these results have thus validated the efficacy and specificity of dlic1 MO and suggest that *dlic1* plays a critical role in directional Dld endosome transport in mitotic RGPs. DLIC1 is involved in endosomal transport in cultured human cells (*51*), suggesting that it may be the isoform that engages endosomes as cargoes. Thus, combined pharmacological and genetic perturbation of dynein function, while not affecting the congregation of Notch signaling endosomes toward the cleavage plane, selectively disrupts their asymmetric segregation into the posterior daughter during RGP ACD.

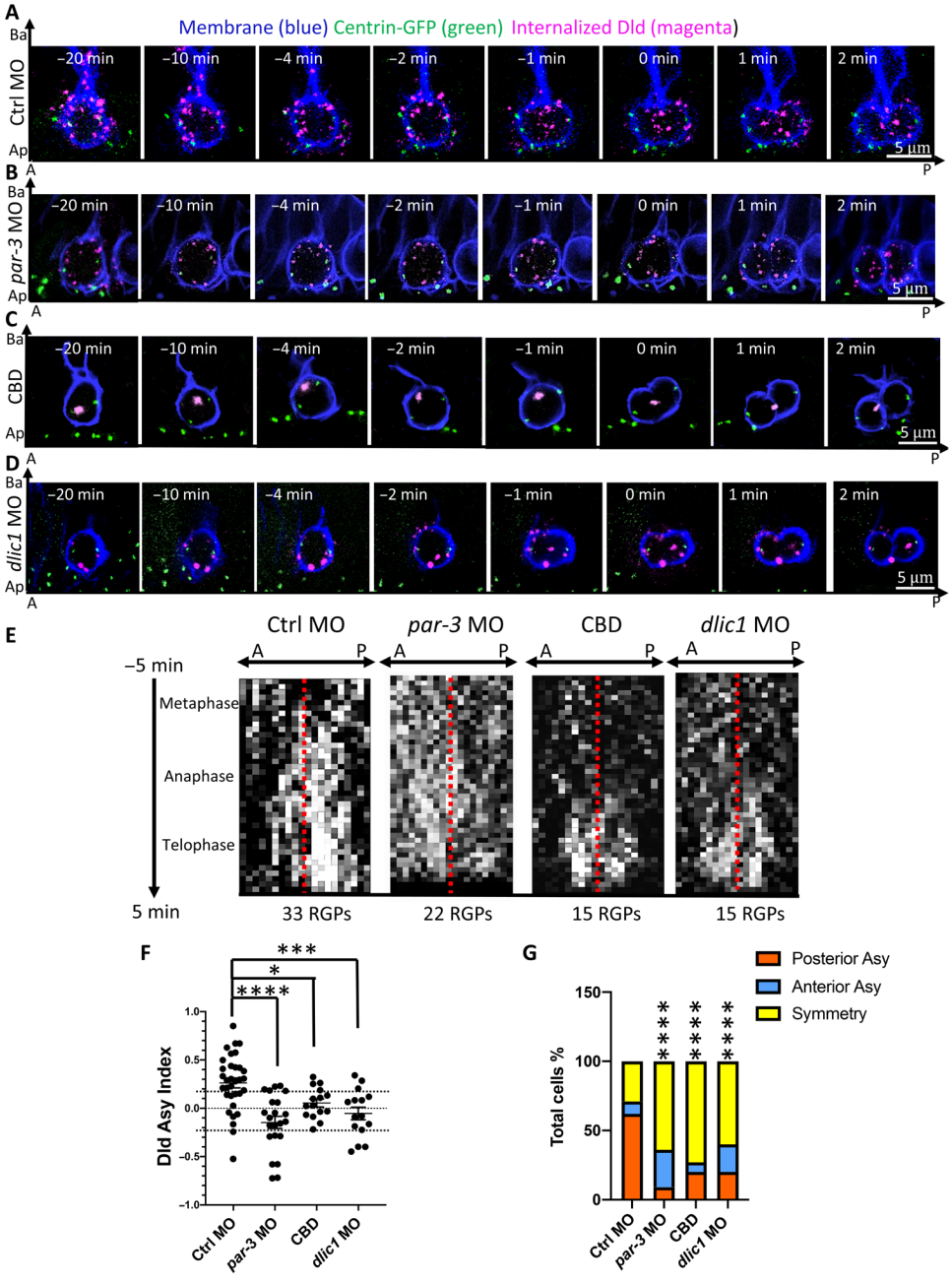

Fig. 3. Dld endosome asymmetry is dependent on Par-3 and the dynein motor machinery. (**A** to **D**) Time-lapse sequence of images showing Dld endosome dynamics in mitotic RGPs from 28-hpf control MO (A) and embryos deficient for *par-3* activity (B), treated with the dynein inhibitor CBD (C), deficient for dynein intermediate light chain 1 (*dlic1*) (D). Centrosomes are labeled with GFP-centrin, and membrane is labeled with Myr-TdTomato reporter. For (A) to (D), all images shown are the MIP of five confocal z-stacks (1−μm z-step). The time interval between each volume of z-stacks is 15 s, and the total acquisition time is 25 min. (**E**) Kymograph of horizontal projection of (A) to (D) showing distribution of all tracked Dld endosomes along the anteroposterior (A-P) axis (*x*) over time (*y*). The red line delineates center point of the axis defined by two centrosomes. (**F**) Scatter plot showing asymmetry indices in telophase RGPs. Thirty-three control MO RGPs were from 25 embryos of eight repeat experiments, 22 *par-3* MO RGPs were from 9 embryos of six repeat experiments, 15 CBD-treated RGPs were from 7 embryos of four repeat experiments, and 15 *dlic1* MO RGPs were from 8 embryos of four repeat experiments. The unpaired two tailed *t* test shows significance between ctrl versus *par-3* MO, $^{****}P < 0.0001$ ($t = 4.706$, df = 53); ctrl MO versus CBD, $^{*}P = 0.0129$ ($t = 2.589$, df = 46); ctrl versus *dlic1* MO $^{**}P = 0.0007$ ($t = 3.645$, df = 46). Mean with SEM is shown for each group. (**G**) Bar graph showing the percentage of RGPs with different patterns of internalized Dld distribution. Disruption of either Par-3 or dynein activity results in a significant decrease of asymmetric posterior Dld segregation. $^{****}P < 0.0001$, χ^2 test (chi-square = 95.62, df = 6).

Par-3 and Dld endosomes are preferentially cosegregated to the posterior daughter following RGP division

Having established an essential role of Par-3 and the dynein motor in polarizing the distribution of Dld endosomes during RGP ACD, we next asked how they might perform such function. In both invertebrates and vertebrates, Par-3 protein displays prominent cortical asymmetry and is widely considered to function at the cell cortex during ACD (*19*, *40*, *52*, *53*). To understand how Par-3 cortical asymmetry relates to polarized Dld endosome dynamics, we performed in vivo time-lapse imaging to simultaneously track the dynamics of Par-3 and internalized Dld in dividing RGPs. Par-3-GFP, which is shown fully functional through rescue experiments (fig. S6) (*41*), was used as a live reporter.

Previous studies in mammalian forebrain cortical RGPs find that the daughter cell inheriting a greater amount of Par-3 develops high Notch activity and remains a RGP, whereas the daughter cell inheriting less Par-3 harbors low Notch activity and adopts an intermediate progenitor or neuronal fate (*27*). In contrast, in the developing zebrafish caudal hindbrain and anterior spinal cord (from 20 to 30 hpf), Par-3 is reported to segregate into the neuronal daughter following neural precursor ACD (*19*). These differences could be related to the differences in species or due to spatiotemporal heterogeneity of progenitors.

To determine the nature of Par-3 and Dld dynamics in the developing zebrafish forebrain RGPs, we microinjected the mRNAs encoding Par-3-GFP and histone H2B-monomeric RFP (H2B-mRFP) (for marking chromosomes) into 1 cell of 16- to 32-cell stage embryos to achieve sparse labeling; the Dld antibody was subsequently microinjected into the brain ventricle at ~24 hpf. Time-lapse imaging was performed at ~28 to 30 hpf. We found that, during prophase and metaphase, Par-3 was prominently localized to the apical cortex (Fig. 4A). As the cell cycle progressed, beginning around anaphase, cortical Par-3 shifted more toward the posterior. Symmetric segregation (Fig. 4B) or asymmetric segregation of Par-3 and Dld to the anterior daughter (Fig. 4C) was also observed.

Among 54 RGPs examined, most (64.8%) showed posteriorly enriched Par-3 at the telophase (Fig. 4D). Further quantifications of both internalized Dld and Par-3 at the telophase stage showed that most of the RGPs (59.2%) segregated both Par-3 and Dld into the posterior daughter (Fig. 4D). These observations are consistent with the heterogeneity of RGP behavior or, alternatively, reflecting, to a certain extent, the noise introduced by mosaic Dld labeling. Nevertheless, these results show clearly that, following RGP division in the developing forebrain, Par-3 preferentially cosegregates with Dld endosomes to the posterior daughter that is Notch^{hi} (as shown in Fig. 2).

Cytoplasmic Par-3 decorates Dld endosomes and is required to recruit Dlic1

Notably, in dividing RGPs, some weak Par-3-GFP signal appeared to be present in the cytoplasm (e.g., Fig. 4A; 3 min). While previous studies are focused on the cortical Par-3, which is much more abundant and considered to be the active form, we were intrigued by the possible presence and function of cytosolic Par-3. To verify the cytosolic presence of Par-3 protein, we used an anti–Par-3 antibody, the specificity of which was validated by both Western blot and immunofluorescence (IF) labeling on the *par-3* morphants without or with MO-insensitive Par-3-GFP mRNA coinjection (fig. S8). While live imaging uses a reporter to uncover protein dynamics and

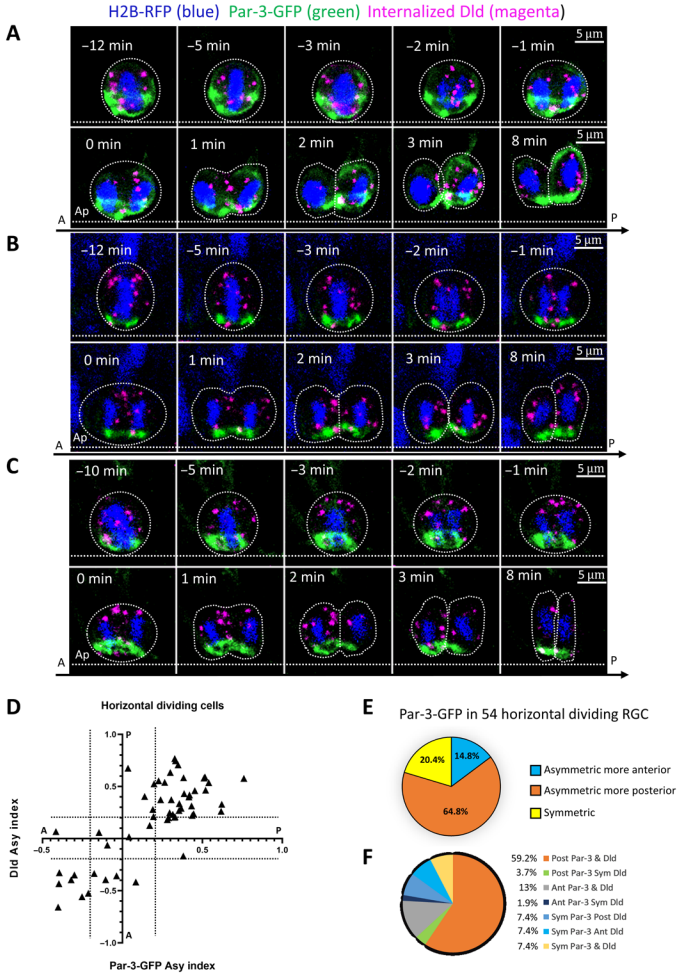

Fig. 4. Preferential segregation of Par-3 and internalized Dld to the posterior daughter following horizontal RGP division. Time-lapse sequence of images showing the dynamics of internalized Dld and Par-3-GFP in mitotic RGPs. DNA is marked by H2B-RFP (pseudo-colored in blue). Time = 2 min denotes telophase when asymmetry indices are calculated. (**A**) Both internalized Dld and Par-3-GFP are asymmetrically segregated to the posterior daughter shortly after division. (**B**) Both internalized Dld and Par-3-GFP appear symmetrically distributed shortly after division. (**C**) Both internalized Dld and Par-3-GFP appear asymmetrically segregated into the anterior daughter shortly after division. For (A) to (C), all images shown are the maximum MIP of five confocal z-stacks (1-μm z-step). The time interval between each volume of z-stacks is 30 s, and the total acquisition time is 30 min. (**D**) Quantification. Left: The asymmetry indices of Par-3-GFP (*x* axis) and internalized Dld (*y* axis) in 54 horizontally dividing RGPs. The dotted lines indicate the threshold of |0.2| for calling asymmetry. Right: Pie charts show the percentage of RGPs with different patterns of Par-3-GFP (top), and Par-3-GFP and internalized Dld (bottom) in 54 horizontally dividing RGPs. Most of the RGPs (64.8%) asymmetrically segregate Par-3 to the posterior daughter. Likewise, most of the RGPs (59.2%) asymmetrically segregate both Par-3 and Dld to the posterior daughter. Other minor classes of RGPs displaying different patterns of segregation might reflect real biological heterogeneity or noise due to mosaic nature of Dld labeling. The 54 RGPs are from 15 embryos in eight repeat experiments.

can be limited in detecting lowly expressed proteins, IF labeling detects endogenous proteins on fixed-sample preparations. Depending on the quality of antibodies and the accessibility of antigens, IF labeling can offer higher sensitivity than live imaging. co-IF labeling

of Par-3, Dlic1, and Dld detected punctate Par-3 immunoreactivity in the cytosol that appeared in close proximity to Dlic1 and Dld immunoreactivity (Fig. 5A and fig. S8).

Analyses of protein colocalization with organelles such as endosomes require specific methods, as the fluorescence signals may not appear to exactly overlap because of the size of the organelle (average endosome diameters of 250 to 1000 nm). Using such method that is shown to work well for quantifying colocalization of proteins with endosomes (*24*, *54*), we analyzed colocalization of these proteins in the cytoplasmic area in between two nuclei of the anaphase/telophase RGPs (Fig. 5B). At this image resolution, ~60% of total Par-3 immunoreactivity colocalized with Dlic1, whereas about 30% of total Dlic1 immunoreactivity colocalized with Par-3. This difference was expected given the broad role of Dlic1 in other dynein-mediated processes. It was further observed that the colocalization of Dld with Dlic1 was significantly decreased in *par-3*–deficient embryos, which was rescued by Par-3-GFP mRNA injection (Fig. 5B). This observation suggests an essential role of Par-3 in localizing Dlic1 (in turn, the dynein motor) to Dld endosomes.

To visualize at high resolution the cytoplasmic Par-3 in relationship to Dld endosomes and Dlic1, we applied LR-ExM. ExM physically expands biological samples to enable nanoscale superresolution via diffraction-limited confocal microscopy (*55*, *56*). LR-ExM further overcomes the limitation of signal loss associated with traditional ExM and enables high-efficiency protein labeling using an engineered set of trifunctional anchors (*36*). Twenty-four– to 28-hpf embryos expressing Par-3-GFP and with internalized Dld were processed for immunolabeling of GFP and Dlic1 followed by LR-ExM. In addition to the cortex, Par-3-GFP was detected in the cytosol in close proximity to Dlic1 and Dld (Fig. 5C). The ring-shaped distribution patterns of Dlic1 and Par-3 together with the diameter of the ring suggest that they decorate Dld endosomes. We also performed LR-ExM by immunolabeling of endogenous Par-3. The results showed similar colocalization of endogenous Par-3 and Dlic1 on Dld endosomes (fig. S9A). Quantification of colocalization after LR-ExM (Fig. 5D) showed patterns that were largely consistent with those observed while analyzing low-magnification images (Fig. 5B).

Last, conventional in vivo coimmunoprecipitation (co-IP) was performed to determine whether Par-3, Dlic1, and Dld could be detected in protein complexes. One- to 2-day-old zebrafish embryos were homogenized and incubated with each of the antibodies against Dld, Dlic1, or Par-3. The corresponding immunoprecipitants were then probed with each of these antibodies by Western blotting (fig. S9B). The results showed that IPing Dld was able to co-IP Par-3 and Dlic1; likewise, IPing Par-3 or Dlic1 was able to co-IP other two proteins. These results provide further biochemical validation that Dld, Dlic1, and Par-3 are associated in complexes in vivo.

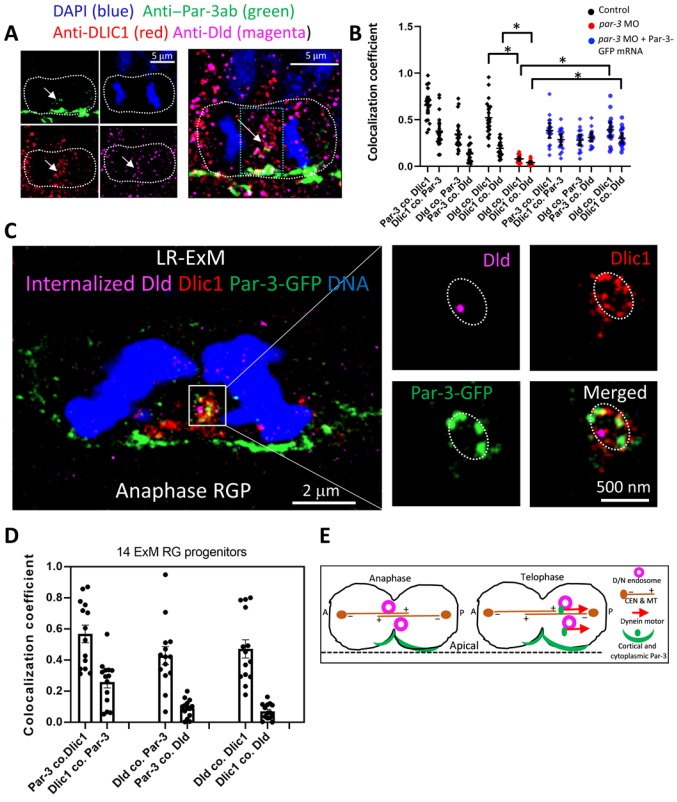

Fig. 5. Cytosolic Par-3 together with Dlic1 decorates Dld endosomes. (**A**) Immunostained anaphase RGP. The green box denotes the area for colocalization analysis (60 × 100 pixels, 0.126-μm pixel size). The white arrows indicate the overlapped cytosolic staining. The MIP of 10 *z*-planes (0.2-μm z-step) is shown. (**B**) Quantification of colocalization coefficients (see Materials and Methods) in RGPs. Dld and Dlic1 colocalization is significantly reduced in the *par-3*–deficient (*par-3* MO) RGPs (n = 18, from six embryos of four repeat experiments) compared with control RGPs (n = 20, from five embryos of four repeat experiments). *P < 0.0001 (Dld co. Dlic1, t = 9.56 and df =36; Dlic1 co. Dld, t = 7.27 and df = 36), unpaired two-tailed t test. In the *par-3* knockdown RGPs rescued with Par-3-GFP mRNA (*par-3* MO + Par-3-GFP mRNA, n = 17, from eight embryos of four repeat experiments), Dld and Dlic1 colocalizations are significantly restored. *P < 0.0001 (Dld co. Dlic1, t = 8.252 and df = 33; Dlic1 co. Dld, t =10.57 and df = 33), unpaired two-tailed t test. Mean with SEM is shown. (**C**) Left: LR-ExM of anaphase RGP from 28-hpf embryo (*par-3*-GFP mRNA injected at 16-cell stage and anti–Dld-Atto647 uptake at 26 hpf). Scale bars denote the real biological size. The MIP of 10 *z*-planes is shown. Right: Enlarged view (MIP of four *z*-planes) of the endosomal structure (dotted ring-like) containing Dld. Z-step = 0.26 μm. (**D**) Statistics of the colocalization coefficient of anti–Par-3, anti-Dlic1, and internalized Dld fluorescence in 14 RGPs (from six embryos of four repeat experiments) processed by LR-ExM. Mean with SEM is shown. (**E**) Summary model. D/N, delta and Notch; CEN, centrosome; MT, microtubule.

DISCUSSION

The evolutionarily conserved polarity regulator Par-3 is required for differential activity of Notch signaling in daughter cells of asymmetrically dividing RGPs (*20*), but the underlying mechanisms are unclear. Using in vivo time-lapse imaging and ExM, in combination with molecular genetics, pharmacological, and biochemical approaches, we have uncovered a role of cytoplasmic Par-3 together with the dynein motor in polarized transport of Dld endosomes (Fig. 5E). This study, together with previous work (*24*), reveals an evolutionarily conserved role of Par-3 in polarizing Notch signaling endosomes. However, Par-3 appears to do so through distinct mechanisms: In *Drosophila* SOPs, Par-3 is previously shown to regulate central spindle asymmetry (*24*); here, we show that in zebrafish RGPs, Par-3 in the cytoplasm engages dynein in polarized transport of endosomes. It is worth noting that a role of Par-3 in regulating central spindle asymmetry has not been investigated in zebrafish; likewise, a role of Par-3 in dynein-mediated polarized transport of Notch signaling endosomes has not been examined in *Drosophila* SOPs. Therefore, future studies are needed to determine whether

convergence of these mechanisms can be observed in different cellular contexts.

Similar species-related differences have also been observed in terms of polarized segregation of cortical Par-3. In the developing mammalian cortex (part of the forebrain), the daughter cell that inherits a greater amount of Par-3 is suggested to develop higher Notch signaling activity (*27*). However, in the developing zebrafish caudal hindbrain and anterior spinal cord, Par-3 is reported to be segregated to the neuronal daughter during the ACD that generates a progenitor and a neuron (*19*). Our studies of the developing zebrafish forebrain uncover that Par-3 and Dld endosomes are preferentially cosegregated into the posterior daughter in horizontally dividing RGPs. Using three independent approaches (cell position tracking, referencing Mib distribution, and direct visualization with the Notch activity reporter), we have demonstrated that the posterior daughter is preferentially Notch^{hi}. Thus, horizontally dividing zebrafish forebrain RGPs are similar to the mammalian cortical RGPs in their patterns of cosegregating cortical Par-3 and Notch activity. Future studies are needed to understand the relationship between Par-3 and Notch activity in other cell types (e.g., hindbrain and spinal cord) in zebrafish.

During ACDs studied across different metazoan species, Par-3 displays prominent cortical localization (*19*, *40*, *52*, *53*). This cortical Par-3 has received much attention as key to establishing polarity (e.g., by sequestering atypical protein kinase C) (*31*, *57*). Cytoplasmic Par-3, released from the membrane via phosphorylation by Par-1 (*58*–*61*), has been considered a largely nonfunctional form in the context of polarity regulation. Being able to visualize Par-3 in the cytoplasm in association with the dynein motor and Dld endosomes as we have done in this study suggests a direct role of cytoplasmic Par-3 in actively localizing intracellular determinants. Cytoplasmic Par-3 has been associated with adverse cancer prognosis in clinical settings (*62*), further suggesting that this form of Par-3 and its dynamic relationship with the cortex-associated oligomeric ensemble deserve more attention in future studies.

MATERIALS AND METHODS

Experimental design

Mitotic RGPs in the developing zebrafish forebrain during active neurogenesis were analyzed using a combination of in vivo time-lapse imaging, molecular genetics, pharmacology, biochemistry, and other advanced microscopic methods, which has uncovered a novel role of cytoplasmic Par-3 in recruiting dynein and actively localizing intracellular determinants.

Zebrafish strains and maintenance

Wild-type (WT) embryos were obtained from natural spawning of AB adults, staged, and maintained according to established protocols (*63*). Embryos were raised at 28.5°C in 0.3× Danieau's embryo medium (30× Danieau's embryo medium contains 1740 mM NaCl, 21 mM KCl, 12 mM $MgSO_4{\cdot}7H_2O$, 18 mM $Ca(NO_3)_2$, and 150 mM Hepes buffer). Embryonic ages were described as hpf. To prevent pigment formation, 0.003% phenylthiourea (PTU) was added into the medium at 24 hpf. The following zebrafish mutants and transgenic lines were used: *mib*^{ta52b} (*35*), *Tg [ef1a:Myr-Tdtomato]* and *Tg[ef1a:H2B-RFP]* (*64*), and *Tg [her4.1-RFP]* (*38*). All animal experiments were approved by the Institutional Animal Care and Use Committee at the University of California, San Francisco, USA.

Morpholinos

Knockdown experiments were carried out using previously characterized translational blocking antisense MOs: *pard3ab/par-3* MO (5′-TCA AAG GCT CCC GTG CTC TGG TGT C-3′) (*19*, *20*, *41*, *65*), *dync1li1/dlic1* MO (5′-GTG TAT TTC TGC CCG TCG TCG CCA T-3′), and *dync1li2/dlic2* MO (5′-TTC TTC TCT AAA ACG GGA GCC ATC T-3′) (*49*). Standard control MO (5′-CCT CTT ACC TCA GTT ACA ATT TAT A-3′) was used as injection controls (Gene Tools). All MOs were stored at 300 mM in distilled water. For microinjection, ~4 nl of the diluted MO at 100 mM in the injection mixture containing 0.05% phenyl red (corresponding to 4 ng of MOs) was injected into the yolk of one- to four-cell stage embryos.

Pharmacology

Zebrafish embryos were treated with the dynein inhibitor CBD [Calbiochem via Sigma-Aldrich, 250401-10MG; 2.5 μM in 0.1% dimethyl sulfoxide (DMSO), 0.3× Danieau's buffer] from 18 to 24 hpf. Vehicle (DMSO)–treated control and CBD-treated embryos were then embedded in 1.2% low–melting point agarose in the Danieau medium, supplemented with 2.5 μM CBD and 0.003% tricaine, and subjected to Dld antibody uptake assay and in vivo time-lapse imaging.

DNA plasmids and complementary DNA preparation

Plasmid DNAs (*pCS2-H2B-mRFP*, *pCS2-mib-GFP*, *Pef1a-gal4*, and *Puas-E1b-EGFP*) were prepared as previously described (*20*, *39*). *pCS2-par-3-GFP* plasmid was a gift from J. von Trotha (*66*). *pCS2-GFP-centrin* plasmid was a gift from W. A. Harris (*67*). For *mib-GFP*, GFP is at the 3′ end of Mib protein. For *par3-GFP*, GFP is at the 3′ end of Par-3 protein. For *GFP-centrin*, GFP is at the 5′ end of centrin. *pCS2*$^{+}$*-dlic1* was made by cloning the *dlic1* complementary DNA (ensemble: ENSDARG00000098317) with codon-optimized sequence to avoid binding by the *dlic1* MO. The total RNA from 10 larvae of 5 dpf was extracted and purified by using the RNAqueous-Micro Total RNA Isolation Kit (Invitrogen, AM1931). The pair of primers used for reverse transcription polymerase chain reaction is 5′-ATT CAT GGA TCC ATG GCC ACC ACC GGA CGC AAC ACT TTA CTA TCG GTT AGC ACA AAT G-3′ and 5′-AAT ACT CTC GAG TCA GGA TTT GTC GTT TTC AGC AGG G-3′, which contain the restriction enzyme sites of Bam HI and Not I for the digestion and ligation with the *pCS2*$^{+}$ vector plasmid.

mRNA synthesis and microinjection

Plasmids (*pCS2-H2B-mRFP*, *pCS2-mib-GFP*, *pCS2-par-3-GFP*, and *pCS2-GFP-centrin*) were linearized by the restriction enzyme Not I digestion. Not I–linearized plasmids were purified (QIAquick Gel Extraction Kit), and the 5′-capped mRNAs were synthesized using the SP6 mMessenger mMachine Kit (Ambion). For *GFP-centrin*, *H2B-mRFP*, *mib-GFP*, and *par-3-GFP* mRNA mRNA injection, 4-nl mRNAs at 0.2 to 0.5 μg/μl were mixed with an equal volume of injection buffer containing 0.05% phenyl red and injected into the yolk of a one- to four-cell stage embryos. For *par-3-GFP* mRNA injection, the mRNAs were injected into single cells at the 32- to 64-cell stages to obtain mosaic expression. All injections were done with an injector (WPI PV830 Pneumatic Pico Pump) and a micromanipulator (Narishige, Tokyo, Japan).

Anti-Dld antibody uptake assay

Anti-mouse immunoglobulin G (IgG)–Atto647N (Sigma-Aldrich, 50185) was used for labeling the mouse monoclonal anti-Dld

antibody (Abcam, ab73331). For antibody conjugation, 1 μl of anti-Dld antibody (0.5 mg/ml) was mixed with 2.5 μl of anti-mouse IgG-Atto647N antibody (1 mg/ml) and incubated at room temperature for 30 min or on ice for 2 to 3 hours. After incubation, 2.5 μl of blocking buffer [mouse IgG (10 mg/ml) with 5 mM azide] and 0.5 μl of 0.5% phenol red (Sigma-Aldrich, P0290) were added for blocking the unconjugated anti-mouse IgG-Atto647N and vortexed thoroughly. Mixtures without anti-Dld antibody were used as control. Before microinjection, 24- to 26-hpf embryos were anesthetized in the Danieau medium supplemented with 0.003% tricaine followed by embedding in 1.2% low–melting point agarose. Ten nanoliters of labeled Dld antibody was injected into the hindbrain ventricle. The phenol red indicator serves to show the diffusion of antibody mixture into the forebrain ventricle. The injected embryos were then released from agarose and cultured in the Danieau medium for 2 hours before imaging.

Brain ventricle–targeted electroporation of plasmid DNAs

Pef1a-gal4 and *Puas-E1b-EGFP* plasmids were mixed at 500 ng/μl for each, and about 20 nl of mixture was microinjected into the hindbrain ventricles of 20- to 22-hpf *Tg [her4.1-RFP]* embryos embedded in 1.2% low–melting point agarose. The electroporation setting and procedures were according to previously established protocols (*39*). Electroporated embryos were released from agarose and transferred to a fresh dish of embryonic medium containing 0.003% PTU and incubated at 28.5°C. Electroporated embryos were checked under a fluorescent stereo microscope after 6 to 8 hours. The embryos with sparsely GFP-labeled RGPs were subjected to the Dld antibody uptake assay followed by in vivo time-lapse imaging.

Antibodies, Western blotting, and immunocytochemistry

Primary antibodies used in this study were as follows: mouse anti-Dld [Abcam, ab73331; Research Resource Identifier (RRID): AB_1268496; lot GR115501-3; 1:200 dilution for immunostaining] (*20*), chicken anti-GFP (Abcam, ab13970; RRID: AB_300798; lot GR3190550-20; 1:500 dilution for immunostaining), rabbit anti–Par-3 (Millipore 07-330; RRID: AB_2101325; lot 3322358; 1:500 for immunostaining) (validated in this study), guinea pig anti–DLIC-Cter (a gift from T. Uemura; 1:100 for immunostaining and 1:500 for Western blotting, validated in this study) (*50*), and rabbit anti–α-tubulin (Santa Cruz Biotechnology, SC-12462; RRID: AB_2241125; lot A2907; 1:1000 for Western blotting).

Secondary antibodies used for IF labeling were as follows: Alexa-conjugated goat anti-rabbit (Alexa 568; Invitrogen, A11011; RRID: AB_143157; lot 792518), goat anti-chicken (Alexa 488; Invitrogen, A11039; RRID: AB_142924; lot 2020124), goat anti-mouse (Alexa 488; Invitrogen, A11002; RRID: AB_2534070; lot 1786359), goat anti–guinea pig (Alexa 488; Invitrogen, A11073; RRID: AB_2534117; lot 46214A), or donkey anti–guinea pig (Alexa 647; the Jackson laboratory, 706-605-148; RRID: AB_2340476; lot 102649-478). All were used at 1:1000 dilution.

Secondary antibodies used for Western blotting were as follows: Amersham ECL donkey anti-rabbit IgG horseradish peroxidase (HRP; GE Healthcare, NA934V; RRID: AB_772211; lot 16921443) and rabbit anti–guinea pig IgG (H + L) HRP (Sigma-Aldrich, A5545; RRID: AB_258247). All were used at the 1:2000 dilution.

Secondary antibodies used for trifunctional linker conjugation in LR-ExM were as follows: goat anti–guinea pig IgG (H + L) unconjugated secondary antibody (Invitrogen, A18771; RRID: AB_2535548), goat anti-rabbit IgG (H + L) cross-adsorbed unconjugated secondary antibody (Invitrogen, 31212; RRID: AB_228335), and goat anti-chicken IgY (H + L) unconjugated secondary antibody (Invitrogen, A16056; RRID: AB_2534729).

For Western blotting, lysates from 15 to 20 28-hpf embryos were homogenized in 80 μl of SDS sample buffer; 15 μl of lysate was used for SDS–polyacrylamide gel electrophoresis (Bio-Rad). Proteins were transferred to a Hybond nitrocellulose membrane by a semidry blotting technique with a Turbo-transblotting cell (Bio-Rad) and detected with appropriate antibodies as previously described (*68*). After the HRP-conjugated secondary antibody incubation, the samples were visualized using the SuperSignal West Dura Extended Duration Substrate (Thermo Fisher Scientific) with the LI-COR Western blotting detection system (LI-COR Biosciences).

For the preparation of cryosections, 28-hpf embryos were fixed overnight at 4°C in phosphate-buffered saline (PBS) buffer with 4% paraformaldehyde. Fixed embryos were washed and incubated in PBS buffer containing 30% sucrose overnight at 4°C. Embryos were then transferred to plastic molds, with the sucrose buffer removed and optimum cutting temperature (OCT) (Tissue-Tek) added. After orienting the embryos to proper positions in the mold, the block was frozen on dry ice. Blocks can be stored at −80°C up to several months. Frozen blocks were then cut into 20-μm sections on a cryostat (Leica) and mounted on Superfrost Plus slides (Thermo Fisher Scientific). The slides were dried at room temperature for 2 to 3 hours and then stored at −80°C until use.

For immunocytochemistry, samples were first washed and preincubated in PBS containing 0.1% Tween 20 or 0.25% Triton X-100 (PBS-T; pH 7.4) with 1% DMSO and 5% natural goat serum at 4°C overnight or longer. They were then incubated with primary antibodies in the preincubation solution (PBS-T with 5% natural goat serum) overnight at 4°C. The samples were then washed thoroughly with PBS-T five times × 10 min each time, followed by incubation in Alexa-conjugated goat anti-rabbit (Alexa 568), goat anti-chicken (Alexa 488), goat anti-mouse (Alexa 488), or goat anti–guinea pig (Alexa 647) secondary antibodies (diluted 1:1000) in the preincubation solution for over 2 hours at room temperature or overnight at 4°C. The samples were washed with PBS-T twice for 10 min each, thrice with PBS for 10 min each, and once with 50% glycerol in PBS for 1 hour, followed by infiltration overnight in 80% glycerol/PBS before imaging. Imaging was done using a confocal microscope (Nikon CSU-W1 Spinning Disk/confocal microscopy) with a 100× oil immersion objective. The z-step of the imaging stack is 0.26 μm.

Time-lapse in vivo imaging

Time-lapse in vivo imaging was done using a confocal microscope (Nikon CSU-W1 Spinning Disk/High Speed Widefield confocal microscopy) with a 40× water immersion objective. Embryos were mounted with 1.2% low–melting point agarose (0.3× Danieau medium and 0.003% tricaine) in glass-bottom culture dishes (MatTek; 35 mm) with the dorsal forebrain facing the coverslip.

For in vivo time-lapse imaging of internalized Dld, Mib-GFP, or Par-3-GFP in dividing RGPs of *Tg [ef1a:Myr-Tdtomato]*, z-stacks with 20 to 30 *z*-planes were acquired consecutively at a 1-μm z-step for each embryonic forebrain region. The exposure time for each fluorescent channel was set at 100 ms by choosing the sequential channel scanning mode for each *z*-plane. The interval between each z-stack ranged from 12 to 30 s, depending on the z-stack settings of the samples. Usually, 80 volumes of z-stacks were captured for each time-lapse imaging, and the duration spanned about 30 min.

For long-term imaging, embryos were placed on a temperature-controlled stage set at 28.5°C. For imaging Notch activity in paired daughter cells using *Tg[her4.1-RFP]* embryos, a GFP reporter plasmid was electroporated into the hindbrain region to label individual RGPs as this transgenic line was reported to better recapitulate Notch activity in the hindbrain than in the forebrain (*38*). Z-stacks with 50 to 60 *z*-planes were acquired consecutively with a 1-μm z-step for each volume. The scanning interval between volumes of z-stacks was set at 6 min. The exposure time for each channel was set at 100 ms for each *z*-plane as described above. For each embryo, 100 to 120 volumes of z-stacks were captured lasting ~12 hours. Data presented in figure panels corresponded to maximum intensity projections of 5 to 10 *z*-planes with 1-μm z-step size, representing the approximate size of RGP.

Label retention expansion microscopy

LR-ExM was performed on cryosections of a 28-hpf embryonic forebrain. Chicken anti-GFP antibody (for detecting Par-3-GFP) or rabbit anti–Par-3 antibody (for detecting endogenous Par-3) and guinea pig anti–Dlic-Cter antibody were used, in conjunction with visualizing Dld (either internalized Atto-labeled Dld or endogenous Dld labeled with mouse anti-Dld antibody). Buffers were prepared as previously described with modifications needed for processing in vivo tissue samples (*36*). The forebrain sections were blocked in blocking buffer, PBS containing 0.1% Triton X-100 (PBS-T, pH 7.4) with 5% natural goat serum overnight at 4°C. The slides were then incubated with primary antibodies in the preincubation buffer overnight at 4°C as described in the immunocytochemistry section above. After washing off primary antibodies, tissue sections were incubated with trifunctional linkers {*N*-hydroxysuccinimide (NHS)–methacrylamide (MA)-biotin–conjugated anti-chicken (or anti-rabbit) IgG (for visualizing Par-3), and NHS-MA-digoxigenin (DIG)–conjugated anti–guinea pig IgG (for visualizing Dlic1) [stock (200 mg/ml), dilute 1:100 before use]} in the preincubation buffer overnight at 4°C in the dark. After washes in PBS four times (5 min each) in the dark, freshly prepared 40 μl of gelation solution was added on each section to cover the whole-tissue sample. The gelation solution was prepared by deoxygenizing the gel monomer solution using a vacuum pump for over 15 min before adding tetramethylethylenediamine (TEMED) and ammonium persulfate (APS), to enhance the effects of trifunctional linkers. The gelation solution–covered samples, protected from light, were incubated in a humidity chamber and allowed to undergo gelation at 37°C for 1 hour. The gelated samples were incubated in the digestion buffer [proteinase K (8 U/ml) in 50 mM tris (pH 8.0), 1 mM EDTA, and 0.5% Triton X-100] on the slides 4 hours at 37°C or overnight at room temperature. At least 10-fold excess volume of digestion buffer was used. Sufficient digestion enabled sections embedded in gels to slide off the glass surface. The gels were washed with excess volume of 150 mM NaCl in six-well plates (black-walled plates, CellVis P06-1.5H-N), at least 5 ml in each well four times, 20 to 30 min each time. After washing off the digestion buffer, the gel samples were incubated in the staining buffer [10 mM Hepes and 150 mM NaCl (pH 7.5)] with 3 to 5 μM Alexa Fluor 488–streptavidin, 3 to 5 μM goat anti-digoxigenin/digoxin Dylight 594, anti-mouse Atto647N (1:500), and 4′,6-diamidino-2-phenylindole (1:1000) for 24 hours at 4°C in the dark. Last, the gels were washed four times with milli-Q water (30 min for each wash) at 4°C in the dark. The gel expanded approximately four times of the original sample size after washing and was ready for imaging in the well under the confocal microscope (Nikon CSU-W1 Spinning Disk/High-Speed Widefield confocal microscopy) with a 60× water immersion objective. The excess water in the well was removed to keep the gel-embedded samples adhered to the glass dish bottom. For immobilization of the gel, 2% low–melting point agarose was added onto the edge of the gel-embedded samples before imaging. The scanning z-step is 0.26 μm.

Image analyses

All the confocal imaging stacks were captured and processed using Micro-Manager 2.0 gamma (μManager, University of California) and ImageJ. For generating kymographs of internalized Dld in dividing RGPs, maximum intensity projection of five to seven *z*-planes (1-μm z-step) was applied to the three-dimensional image stacks to cover the entire RGP. Each RGP at every time frame was manually segmented according to the cell membrane labeling. Each single Dld endosome was located from all frames using a Gaussian fitting algorithm assisted with the ImageJ-embedded plugin TrackMate (*69*), by choosing "LoG" detector and setting the "estimated diameter" to be about 8 pixels and "threshold" to be about 3 pixels (pixel width and pixel height are 0.164 μm, and voxel depth is 1 μm). The Linear Assignment Problem (LAP) tracker was adopted without "allow gap closing." All Dld endosomes tracked on each image frame were previewed and compared to the original frame. The threshold parameter was then adjusted on the basis of this visual feedback. The two labeled centrosomes were used to define the anteroposterior (A-P) axis: The anterior centrosome was given the coordinate of 0, and the posterior centrosome was given the coordinate of 1. Each Dld endosome was then projected onto this axis to obtain its relative distance (value between 0 and 1). The relative distances of all tracked Dld endosomes were then used to generate the kymograph, where the grayscale value of each pixel indicates the probability of Dld endosomes appearing at the corresponding location at a given time.

Movies for each RGP used for kymograph analyses were registered spatiotemporally: The spatial registration was done by adopting the center point between two centrosomes as the center of dividing RGPs. The temporal registration was done by adopting the anaphase with the first appearance of cleavage furrow to be $T = 0$ min. The first appearance of the cleavage furrow was also verified in a set of embryos with double labeling of cell membrane and nucleus. Almost all WT (or control MO-injected) RGPs complete their cytokinesis at $T = 2$ min. However, for RGPs in *par-3* MO, *dlic* MO, or CBD-treated embryos, the time from first appearance of the cleavage furrow ($T = 0$ min) to the completion of cytokinesis ($T = 2$ min in control) was variable because of possible cell cycle defects. We therefore normalized this to WT cell cycle by considering the completion of cytokinesis as $T = 2$ min.

Quantification and statistical analysis

The number of times each experiment was repeated was provided in the figures or figure legends. For live imaging, one or multiple RGPs were analyzed from each embryo, depending on the number of mitotic RGPs that were present in each image stack. For immunocytochemistry experiments, multiple sections from individual brains were analyzed. No statistical methods were used to predetermine sample size. Sample size was determined to be adequate on the basis of the magnitude and consistency of measurable differences between groups. No randomization of samples was performed. Embryos used in the analyses were age-matched between control and experimental conditions, and sex cannot be discerned at these

embryonic stages. Investigators were not blinded to chemically or genetically perturbed conditions during experiments. Data are quantitatively analyzed.

Statistical analyses were carried out using Prism 8 version 8.4.2: The mean value with SEM was labeled in the graphs. The two-tailed unpaired *t* test was used to assess significance. To compare the proportions of each cell division orientation (extended data in Fig. 1), normal (*z*) test for proportions (implemented by Python's statsmodels package) (*70*) was used. The chi-square analyses were also applied in Fig. 3 and fig.S6.

Measurement of asymmetry index

The total fluorescence intensity of internalized Dld (or Mib-GFP and Par-3-GFP) in paired daughter cells immediately after abscission (i.e., at telophase of mother RGP division) was measured by ImageJ. To quantitatively describe the distribution, normalized ratio of fluorescence between the two newly formed daughter cells was calculated as follows

$$X = \frac{\frac{\sum_{i=1}^{n}(\mathrm{Dld})\mathrm{P} - \sum_{i=1}^{n}(\mathrm{Dld})\mathrm{A}}{n}}{\sum_{i=1}^{n}(\mathrm{Dld})\mathrm{P} + \sum_{i=1}^{n}(\mathrm{Dld})\mathrm{A}}$$

Σ(Dld)P means total intensity in the posterior daughter cell, and Σ(Dld)A means total intensity in the anterior daughter cell. "0" indicates perfect symmetry, and "1" or "−1" indicates absolute asymmetry (posterior or anterior, respectively). For filtering out potential noise, we defined asymmetry when Σ(Dld)P is 50% more or less than Σ(Dld)A, as has been previously used for quantifying Par-3 asymmetry (*27*) and internalized Dld-containing Sara endosome asymmetry (*25*). It means that when $X \geq 0.2$, Dld endosomes (or Mib-GFP and Par-3-GFP) are considered asymmetric with more in the posterior daughter, and when $X \leq -0.2$, they are considered asymmetric with more in the anterior. The asymmetry index for Par3-GFP included both membrane and cytoplasmic fluorescence.

Colocalization

To measure the colocalization of Dlic1 and Par-3 (or Par-3-GFP), in the context of Dld (either internalized or immunostained) endosomes in the cytosol of dividing RGPs, we adopted the methods as previously described for measuring colocalization in the context of endosomes (*24*, *54*). This method is distinct from conventional, intensity correlation coefficient–based colocalization method, which performs poorly because the membrane of endosomes is organized as a mosaic of domains (*71*).

Immunostained mitotic RGPs were segmented, and maximum intensity projections of 10 consecutive *z*-planes (with 0.26-μm z-step size) were generated, which typically covers the central cytoplasmic area between the nuclei (~2.6 μm). The area of 60 × 100 pixels (1 pixel = 0.064 μm) was then cropped for colocalization analysis using the JACop plugin in ImageJ. The colocalization between each fluorescent channel (i.e., the proportion of each fluorescence colocalized with another) was measured using Manders' coefficients (*72*). We used an optimized *XY* block size of 2 pixels (*54*). To remove potential background noise, the threshold of each channel was set in JACop using a blank area on the image (i.e., without tissue samples) as a negative control. Costes' automatic threshold was further applied for each measurement. Costes' automatic threshold is an algorithm that identifies and removes noise using scatter plotting of randomized images generated from the image under analysis (*73*). It automatically quantifies colocalization without the bias of visual interpretation.

For RGPs from LR-ExM, the maximum intensity projections of 10 consecutive *z*-planes (0.26-μm z-step size scanned with a 60× water immersion objective) were generated. The central cytoplasmic area between the nuclei was then selected, and *XY* block size was defined as 1 pixel for JACop colocalization analyses.

SUPPLEMENTARY MATERIALS

Supplementary material for this article is available at http://advances.sciencemag.org/cgi/content/full/7/24/eabg1244/DC1

View/request a protocol for this paper from *Bio-protocol*.

REFERENCES AND NOTES

1. K. J. Yong, B. Yan, The relevance of symmetric and asymmetric cell divisions to human central nervous system diseases. *J. Clin. Neurosci.* **18**, 458–463 (2011).
2. M. C. Florian, H. Geiger, Concise review: Polarity in stem cells, disease, and aging. *Stem Cells* **28**, 1623–1629 (2010).
3. V. Aranda, M. E. Nolan, S. K. Muthuswamy, Par complex in cancer: A regulator of normal cell polarity joins the dark side. *Oncogene* **27**, 6878–6887 (2008).
4. M. C. Wagner, B. A. Molitoris, Renal epithelial polarity in health and disease. *Pediatr. Nephrol.* **13**, 163–170 (1999).
5. S. Guo, K. J. Kemphues, Molecular genetics of asymmetric cleavage in the early *Caenorhabditis elegans* embryo. *Curr. Opin. Genet. Dev.* **6**, 408–415 (1996).
6. K. J. Kemphues, J. R. Priess, D. G. Morton, N. S. Cheng, Identification of genes required for cytoplasmic localization in early *C. elegans* embryos. *Cell* **52**, 311–320 (1988).
7. L. S. Rose, K. J. Kemphues, Early patterning of the *C. elegans* embryo. *Annu. Rev. Genet.* **32**, 521–545 (1998).
8. B. Goldstein, I. G. Macara, The PAR proteins: Fundamental players in animal cell polarization. *Dev. Cell* **13**, 609–622 (2007).
9. F. Motegi, G. Seydoux, The PAR network: Redundancy and robustness in a symmetry-breaking system. *Philos. Trans. R. Soc. Lond. B Biol. Sci.* **368**, 20130010 (2013).
10. C. Hoege, A. A. Hyman, Principles of PAR polarity in *Caenorhabditis elegans* embryos. *Nat. Rev. Mol. Cell Biol.* **14**, 315–322 (2013).
11. F. Peglion, N. W. Goehring, Switching states: Dynamic remodelling of polarity complexes as a toolkit for cell polarization. *Curr. Opin. Cell Biol.* **60**, 121–130 (2019).
12. M. Inaba, Y. M. Yamashita, Asymmetric stem cell division: Precision for robustness. *Cell Stem Cell* **11**, 461–469 (2012).
13. C. C. Homem, M. Repic, J. A. Knoblich, Proliferation control in neural stem and progenitor cells. *Nat. Rev. Neurosci.* **16**, 647–659 (2015).
14. E. Taverna, M. Götz, W. B. Huttner, The cell biology of neurogenesis: Toward an understanding of the development and evolution of the neocortex. *Annu. Rev. Cell Dev. Biol.* **30**, 465–502 (2014).
15. C. Q. Doe, Neural stem cells: Balancing self-renewal with differentiation. *Development* **135**, 1575–1587 (2008).
16. D. Delaunay, A. Kawaguchi, C. Dehay, F. Matsuzaki, Division modes and physical asymmetry in cerebral cortex progenitors. *Curr. Opin. Neurobiol.* **42**, 75–83 (2017).
17. F. Schweisguth, Asymmetric cell division in the *Drosophila* bristle lineage: From the polarization of sensory organ precursor cells to notch-mediated binary fate decision. *Wiley Interdiscip. Rev. Dev. Biol.* **4**, 299–309 (2015).
18. B. Lu, L. Jan, Y. N. Jan, Control of cell divisions in the nervous system: Symmetry and asymmetry. *Annu. Rev. Neurosci.* **23**, 531–556 (2000).
19. P. Alexandre, A. M. Reugels, D. Barker, E. Blanc, J. D. Clarke, Neurons derive from the more apical daughter in asymmetric divisions in the zebrafish neural tube. *Nat. Neurosci.* **13**, 673–679 (2010).
20. Z. Dong, N. Yang, S.-Y. Yeo, A. Chitnis, S. Guo, Intralineage directional Notch signaling regulates self-renewal and differentiation of asymmetrically dividing radial glia. *Neuron* **74**, 65–78 (2012).
21. S. Singh, D. J. Solecki, Polarity transitions during neurogenesis and germinal zone exit in the developing central nervous system. *Front. Cell. Neurosci.* **9**, 62 (2015).
22. W. A. Liu, S. Chen, Z. Li, C. H. Lee, G. Mirzaa, W. B. Dobyns, M. E. Ross, J. Zhang, S. H. Shi, PARD3 dysfunction in conjunction with dynamic HIPPO signaling drives cortical enlargement with massive heterotopia. *Genes Dev.* **32**, 763–780 (2018).

23. F. Coumailleau, M. Fürthauer, J. A. Knoblich, M. González-Gaitán, Directional Delta and Notch trafficking in Sara endosomes during asymmetric cell division. *Nature* **458**, 1051–1055 (2009).
24. E. Derivery, C. Seum, A. Daeden, S. Loubéry, L. Holtzer, F. Jülicher, M. Gonzalez-Gaitan, Polarized endosome dynamics by spindle asymmetry during asymmetric cell division. *Nature* **528**, 280–285 (2015).
25. S. Kressmann, C. Campos, I. Castanon, M. Fürthauer, M. González-Gaitán, Directional Notch trafficking in Sara endosomes during asymmetric cell division in the spinal cord. *Nat. Cell Biol.* **17**, 333–339 (2015).
26. K. Mizutani, K. Yoon, L. Dang, A. Tokunaga, N. Gaiano, Differential Notch signalling distinguishes neural stem cells from intermediate progenitors. *Nature* **449**, 351–355 (2007).
27. R. S. Bultje, D. R. Castaneda-Castellanos, L. Y. Jan, Y. N. Jan, A. R. Kriegstein, S. H. Shi, Mammalian Par3 regulates progenitor cell asymmetric division via notch signaling in the developing neocortex. *Neuron* **63**, 189–202 (2009).
28. S. E. Williams, S. Beronja, H. A. Pasolli, E. Fuchs, Asymmetric cell divisions promote Notch-dependent epidermal differentiation. *Nature* **470**, 353–358 (2011).
29. S. Artavanis-Tsakonas, M. Rand, R. Lake, Notch signaling: Cell fate control and signal integration in development. *Science* **284**, 770–776 (1999).
30. N. Gaiano, G. Fishell, The role of notch in promoting glial and neural stem cell fates. *Annu. Rev. Neurosci.* **25**, 471–490 (2002).
31. E. Munro, Protein clustering shapes polarity protein gradients. *Dev. Cell* **42**, 309–311 (2017).
32. S. C. Noctor, A. C. Flint, T. A. Weissman, R. S. Dammerman, A. R. Kriegstein, Neurons derived from radial glial cells establish radial units in neocortex. *Nature* **409**, 714–720 (2001).
33. A. Kriegstein, A. Alvarez-Buylla, The glial nature of embryonic and adult neural stem cells. *Annu. Rev. Neurosci.* **32**, 49–84 (2009).
34. K. Tong, M. Wagle, S. Guo, Antibody uptake assay in the embryonic zebrafish forebrain to study notch signaling dynamics in neural progenitor cells in vivo. *Methods Mol. Biol.* **1576**, 273–281 (2019).
35. M. Itoh, C. H. Kim, G. Palardy, T. Oda, Y. J. Jiang, D. Maust, S. Y. Yeo, K. Lorick, G. J. Wright, L. Ariza-McNaughton, A. M. Weissman, J. Lewis, S. C. Chandrasekharappa, A. B. Chitnis, Mind bomb is a ubiquitin ligase that is essential for efficient activation of Notch signaling by Delta. *Dev. Cell* **4**, 67–82 (2003).
36. X. Shi, Q. Li, Z. Dai, A. Tran, S. Feng, A. D. Ramirez, Z. Lin, X. Wang, T. T. Chow, I. B. Seiple, B. Huang, Label-retention expansion microscopy. *BioRxiv* **2019**, 687954 (2019).
37. S. Tozer, C. Baek, E. Fischer, R. Goiame, X. Morin, Differential routing of Mindbomb1 via centriolar satellites regulates asymmetric divisions of neural progenitors. *Neuron* **93**, 542–551.e4 (2017).
38. S. Y. Yeo, M. Kim, H. S. Kim, T. L. Huh, A. B. Chitnis, Fluorescent protein expression driven by her4 regulatory elements reveals the spatiotemporal pattern of Notch signaling in the nervous system of zebrafish embryos. *Dev. Biol.* **301**, 555–567 (2007).
39. Z. Dong, M. Wagle, S. Guo, Time-lapse live imaging of clonally related neural progenitor cells in the developing zebrafish forebrain. *J. Vis. Exp.* **2011**, 2594 (2011).
40. B. Etemad-Moghadam, S. Guo, K. J. Kemphues, Asymmetrically distributed PAR-3 protein contributes to cell polarity and spindle alignment in early *C. elegans* embryos. *Cell* **83**, 743–752 (1995).
41. M. Tawk, C. Araya, D. A. Lyons, A. M. Reugels, G. C. Girdler, P. R. Bayley, D. R. Hyde, M. Tada, J. D. W. Clarke, A mirror-symmetric cell division that orchestrates neuroepithelial morphogenesis. *Nature* **446**, 797–800 (2007).
42. A. J. Blasky, L. Pan, C. B. Moens, B. Appel, Pard3 regulates contact between neural crest cells and the timing of schwann cell differentiation but is not essential for neural crest migration or myelination. *Dev. Dyn.* **243**, 1511–1523 (2014).
43. A. Rossi, Z. Kontarakis, C. Gerri, H. Nolte, S. Hölper, M. Krüger, D. Y. R. Stainier, Genetic compensation induced by deleterious mutations but not gene knockdowns. *Nature* **524**, 230–233 (2015).
44. J. Schmoranzer, J. P. Fawcett, M. Segura, S. Tan, R. B. Vallee, T. Pawson, G. G. Gundersen, Par3 and dynein associate to regulate local microtubule dynamics and centrosome orientation during migration. *Curr. Biol.* **19**, 1065–1074 (2009).
45. S. Mische, Y. He, L. Ma, M. Li, M. Serr, T. S. Hays, Dynein light intermediate chain: An essential subunit that contributes to spindle checkpoint inactivation. *Mol. Biol. Cell* **19**, 4918–4929 (2008).
46. J. H. Yoder, M. Han, Cytoplasmic dynein light intermediate chain is required for discrete aspects of mitosis in *Caenorhabditis elegans*. *Mol. Biol. Cell* **12**, 2921–2933 (2001).
47. S. H. Tynan, A. Purohit, S. J. Doxsey, R. B. Vallee, Light intermediate chain 1 defines a functional subfraction of cytoplasmic dynein which binds to pericentrin. *J. Biol. Chem.* **275**, 32763–32768 (2000).
48. S. L. Reck-Peterson, W. B. Redwine, R. D. Vale, A. P. Carter, The cytoplasmic dynein transport machinery and its many cargoes. *Nat. Rev. Mol. Cell Biol.* **19**, 382–398 (2018).
49. S. Mahale, M. Kumar, A. Sharma, A. Babu, S. Ranjan, C. Sachidanandan, S. V. S. Mylavarapu, The light intermediate chain 2 subpopulation of dynein regulates mitotic spindle orientation. *Sci. Rep.* **6**, 22 (2016).
50. D. Satoh, D. Sato, T. Tsuyama, M. Saito, H. Ohkura, M. M. Rolls, F. Ishikawa, T. Uemura, Spatial control of branching within dendritic arbors by dynein-dependent transport of Rab5-endosomes. *Nat. Cell Biol.* **10**, 1164–1171 (2008).
51. C. P. Horgan, S. R. Hanscom, R. S. Jolly, C. E. Futter, M. W. McCaffrey, Rab11-FIP3 links the Rab11 GTPase and cytoplasmic dynein to mediate transport to the endosomal-recycling compartment. *J. Cell Sci.* **123**, 181–191 (2010).
52. A. Wodarz, A. Ramrath, U. Kuchinke, E. Knust, Bazooka provides an apical cue for Inscuteable localization in *Drosophila* neuroblasts. *Nature* **402**, 544–547 (1999).
53. M. Schober, M. Schaefer, J. A. Knoblich, Bazooka recruits Inscuteable to orient asymmetric cell divisions in *Drosophila* neuroblasts. *Nature* **402**, 548–551 (1999).
54. S. Bolte, F. P. Cordelières, A guided tour into subcellular colocalization analysis in light microscopy. *J. Microsc.* **224**, 213–232 (2006).
55. F. Chen, P. W. Tillberg, E. S. Boyden, Expansion microscopy. *Science* **347**, 543–548 (2015).
56. P. W. Tillberg, F. Chen, K. D. Piatkevich, Y. Zhao, C. C. Yu, B. P. English, L. Gao, A. Martorell, H. J. Suk, F. Yoshida, E. M. DeGennaro, D. H. Roossien, G. Gong, U. Seneviratne, S. R. Tannenbaum, R. Desimone, D. Cai, E. S. Boyden, Protein-retention expansion microscopy of cells and tissues labeled using standard fluorescent proteins and antibodies. *Nat. Biotechnol.* **34**, 987–992 (2016).
57. J. Betschinger, K. Mechtler, J. A. Knoblich, The Par complex directs asymmetric cell division by phosphorylating the cytoskeletal protein Lgl. *Nature* **422**, 326–330 (2003).
58. Z. Yang, B. Xue, M. Umitsu, M. Ikura, S. K. Muthuswamy, B. G. Neel, The signaling adaptor GAB1 regulates cell polarity by acting as a PAR protein scaffold. *Mol. Cell* **47**, 469–483 (2012).
59. F. Motegi, S. Zonies, Y. Hao, A. A. Cuenca, E. Griffin, G. Seydoux, Microtubules induce self-organization of polarized PAR domains in *Caenorhabditis elegans* zygotes. *Nat. Cell Biol.* **13**, 1361–1367 (2011).
60. A. Sailer, A. Anneken, Y. Li, S. Lee, E. Munro, Dynamic opposition of clustered proteins stabilizes cortical polarity in the *C. elegans* zygote. *Dev. Cell* **35**, 131–142 (2015).
61. S. Guo, K. J. Kemphues, par-1, a gene required for establishing polarity in *C. elegans* embryos, encodes a putative ser/thr kinase that is asymmetrically distributed. *Cell* **81**, 611–620 (1995).
62. J. Dagher, F. Dugay, N. Rioux-Leclercq, G. Verhoest, E. Oger, K. Bensalah, F. Cabillic, F. Jouan, S. F. Kammerer-Jacquet, P. Fergelot, C. Vigneau, Y. Arlot-Bonnemains, M. A. Belaud-Rotureau, Cytoplasmic PAR-3 protein expression is associated with adverse prognostic factors in clear cell renal cell carcinoma and independently impacts survival. *Hum. Pathol.* **45**, 1639–1646 (2014).
63. C. B. Kimmel, W. W. Ballard, S. R. Kimmel, B. Ullmann, T. F. Schilling, Stages of embryonic development of the zebrafish. *Dev. Dyn.* **203**, 253–310 (1995).
64. D. Yu, Z. Dong, W. C. Gustafson, R. Ruiz-González, L. Signor, F. Marzocca, F. Borel, M. P. Klassen, K. Makhijani, A. Royant, Y. N. Jan, W. A. Weiss, S. Guo, X. Shu, Rational design of a monomeric and photostable far-red fluorescent protein for fluorescence imaging in vivo. *Protein Sci.* **25**, 308–315 (2016).
65. X. Wei, Y. Cheng, Y. Luo, X. Shi, S. Nelson, D. R. Hyde, The Zebrafish Pard3 ortholog is required for separation of the eye fields and retinal lamination. *Dev. Biol.* **269**, 286–301 (2004).
66. J. W. von Trotha, J. A. Campos-Ortega, A. M. Reugels, Apical localization of ASIP/PAR-3:EGFP in zebrafish neuroepithelial cells involves the oligomerization domain CR1, the PDZ domains, and the C-terminal portion of the protein. *Dev. Dyn.* **235**, 967–977 (2006).
67. F. R. Zolessi, L. Poggi, C. J. Wilkinson, C. B. Chien, W. A. Harris, Polarization and orientation of retinal ganglion cells in vivo. *Neural Dev.* **1**, 2 (2006).
68. X. Zhao, J. Kuja-Panula, M. Sundvik, Y. C. Chen, V. Aho, M. A. Peltola, T. Porkka-Heiskanen, P. Panula, H. Rauvala, Amigo adhesion protein regulates development of neural circuits in zebrafish brain. *J. Biol. Chem.* **289**, 19958–19975 (2014).
69. J. Y. Tinevez, N. Perry, J. Schindelin, G. M. Hoopes, G. D. Reynolds, E. Laplantine, S. Y. Bednarek, S. L. Shorte, K. W. Eliceiri, TrackMate: An open and extensible platform for single-particle tracking. *Methods* **115**, 80–90 (2017).
70. S. Seabold, J. Perktold, statsmodels: Econometric and statistical modeling with python, in *Proceedings of the 9th Python in Science Conference* (SCIPY, 2010), pp. 92–96.
71. J. Gruenberg, The endocytic pathway: A mosa ic of domains. *Nat. Rev. Mol. Cell Biol.* **2**, 721–730 (2001).
72. E. M. Manders, J. Stap, G. J. Brakenhoff, R. van Driel, J. A. Aten, Dynamics of three-dimensional replication patterns during the S-phase, analysed by double labelling of DNA and confocal microscopy. *J. Cell Sci.* **103**, 857–862 (1992).
73. S. V. Costes, D. Daelemans, E. H. Cho, Z. Dobbin, G. Pavlakis, S. Lockett, Automatic and quantitative measurement of protein-protein colocalization in live cells. *Biophys. J.* **86**, 3993–4003 (2004).

Acknowledgments: We thank M. Wagle for technical training on brain ventricle–targeted electroporation; M. Munchua and V. Yuan for excellent animal care; A. Kriegstein, B. Lu, M. Nachury, J. Reiter, and Guo laboratory members for helpful discussions; D. Larsen,

K. Herrington, and UCSF Nikon imaging center for assistance with imaging and data analysis; and T. Uemura for the anti-DLIC antibody. **Funding:** This project was supported by NIH R01NS095734 and R01NS120218 (to S.G.), the UCSF Mary Anne Koda-Kimble Seed Award for Innovation (to X.Z.), The Luis Zeh Fellowship (to J.Q.G.), the Fudan Bio-elite undergraduate program (to K.T.), NIH R01GM124334 and R01GM131641 (to B.H.), and NIH K99GM126136/R00GM126136 (to X.S.). B.H. is a Chan Zuckerberg Biohub Investigator. **Author contributions:** X.Z. and S.G. designed the experiments and interpreted the results. X.Z. performed most of the experiments, J.Q.G. performed live imaging that contributed to Fig. 4, and K.T. performed antibody uptake assay in the *mib*$^{-/-}$ mutant and live imaging that contributed to fig. S1. Q.L., Z.D., X.S., I.B.S., and B.H. assisted with critical steps in establishing LR-ExM on in vivo zebrafish samples. X.C., B.Y., and B.H. assisted with critical steps in image analysis. X.Z. and S.G. wrote the manuscript, with the input from all authors. **Competing interests:** The authors declare that they have no competing interests. **Data and materials availability:** All data needed to evaluate the conclusions in the paper are present in the paper and/or the Supplementary Materials. Additional data related to this paper may be requested from the authors.

Submitted 11 December 2020
Accepted 26 April 2021
Published 11 June 2021
10.1126/sciadv.abg1244

Citation: X. Zhao, J. Q. Garcia, K. Tong, X. Chen, B. Yang, Q. Li, Z. Dai, X. Shi, I. B. Seiple, B. Huang, S. Guo, Polarized endosome dynamics engage cytoplasmic Par-3 that recruits dynein during asymmetric cell division. *Sci. Adv.* **7**, eabg1244 (2021).